Evaporation residue excitation function measurements in ^{50}Ti- and ^{54}Cr-induced reactions with lanthanide targets

D. A. Mayorov, T. A. Werke, M. C. Alfonso, E. E. Tereshatov, M. E. Bennett, M. M. Frey, and C. M. Folden, III

Phys. Rev. C **92**, 054601 — Published 2 November 2015

DOI: 10.1103/PhysRevC.92.054601

Evaporation residue excitation function measurements in ^{50}Ti- and ^{54}Cr-induced reactions with lanthanide targets

D. A. Mayorov[1,2], T. A. Werke[1,2], M. C. Alfonso[1,2], E. E. Tereshatov[1], M. E. Bennett[1,a], M. M. Frey[2,b], C. M. Folden III[1,†]

[1]*Cyclotron Institute, Texas A&M University, College Station, Texas, 77843, USA*
[2]*Department of Chemistry, Texas A&M University, College Station, Texas, 77843, USA*

Cross sections for the production of shell-stabilized evaporation residues in the ^{50}Ti+^{160}Gd, ^{159}Tb, ^{162}Dy and ^{54}Cr+^{162}Dy reactions are reported. The compound nucleus excitation energy range considered principally covers the 4*n* evaporation channel, with segments of the 3*n* and 5*n* channels also measured. The resultant production cross sections are for nuclides with Z = 86–90. From an analysis based on a statistical model, it is concluded that a larger fission probability than that predicted by the Bohr-Wheeler transition-state theory is needed to describe the data. This outcome is attributed to the influence of collective nuclear excitations. Subsequently, the expected stability enhancement against fission due to the influence of the magic N = 126 shell is not evident. The x*n* excitation functions measured in previous experiments in the reactions ^{48}Ca+^{154}Gd,^{159}Tb,^{162}Dy,^{165}Ho are combined with the present data for Z > 20 projectiles to illustrate systematic behavior of measured cross sections as a function of the difference in fission barrier and neutron separation energy.

PACS number(s): 25.70.Gh, 25.70.Jj, 21.10.Ma, 24.10.-i

[a] Present Address: Nuclear Engineering Division, Argonne National Laboratory, Argonne, Illinois 60439 USA
[b] Present Address: Lower Colorado River Authority, Austin, Texas 78744 USA
[†] Corresponding author. Email Address: Folden@comp.tamu.edu

I. INTRODUCTION

An accurate description of the fission process is important in a number of disciplines, e.g., astrophysics, nuclear physics, and nuclear engineering. Although a successful explanation of nuclear fission based on transition-state theory was presented in the seminal work of Bohr and Wheeler in 1939 [1], the significance and extent of some phenomena that alter its purely statistical description remain puzzling. One standing question concerns the influence of shell structure on the stability of a nucleus against disintegration in fission. In a preceding publication [2], ^{48}Ca-induced reactions with lanthanide targets were used to produce shell-stabilized nuclides with Z = 84–87 near the N = 126 shell. A model-dependent analysis of the resulting x*n* excitation functions demonstrated that a fission probability larger than that predicted by the transition-state formula was needed to describe the data. This outcome was attributed to the collective enhancement of level density (CELD) above the fission saddle due predominantly to rotational excitations. The levels of the spherical daughter in the particle evaporation channels are instead enhanced by vibrational excitations. The end result is an increased probability of fission and a reduced evaporation residue (EvR) production cross section. This problem also bears relevance to the synthesis of superheavy elements (SHE) near the predicted spherical neutron shell closure above N = 126, i.e., N = 184 [3, 4]. Attempts to search for nuclides with Z > 118 near this predicted superheavy magic number region have been reported in [5-7], with no relevant decay chains reported to date for Z ≥ 119. Thus, insights on phenomena influencing the synthesis of spherical EvRs are valuable.

Earlier works [8, 9] have noted the lack of a stabilizing influence of the N = 126 shell on the survival probability of compound nuclei (CN) produced in its vicinity. This same conclusion was later supported by measured fission probabilities of electromagnetically excited Z ≈ 88–90 secondary fragments produced in fragmentation of ^{238}U, which were more likely to fission when near the magic N = 126 shell [10]. These fragments were modestly excited, thereby targeting the energy region where shell effects are strongest. More recent experiments showed evidence for the enhancement of the nuclear level density [11] and suppression of the EvR production cross section [12] believed to result from collective phenomena. On the other hand, other works [13, 14] present a more reserved view on the significance of the CELD effect, thus warranting additional research on the outcome from the interplay between nuclear collectivity and level density. In this paper, excitation functions for the production of fissile EvRs in ^{50}Ti- and ^{54}Cr-induced reactions with ^{160}Gd, ^{159}Tb and ^{162}Dy targets were measured, which complement the previous ^{48}Ca work cited above. The higher fissility of the resulting EvRs should make them more sensitive to the influence of CELD. The ^{48}Ca, ^{50}Ti, and ^{54}Cr reactions present a unique series, with scarce prior data available on ^{50}Ti- and ^{54}Cr-induced hot fusion reactions. This is noteworthy, as projectiles with Z > 20 are most promising for the synthesis of the next new element using a heavy-ion fusion-evaporation reaction [6].

II. EXPERIMENTAL METHODS

The experiments were carried out at the Cyclotron Institute at Texas A&M University, with the data acquisition setup previously described in detail in [2, 15]. In several temporally separated experiments, the K500 superconducting cyclotron accelerated beams of $^{50}Ti^{7+}$ and $^{54}Cr^{7+}$ to energies of 4.9 MeV/u and 5.1 MeV/u, respectively. The purchased $^{50}TiO_2$ [(65.8 ± 1.8)% enrichment] underwent CaH_2 reduction [16] to a ^{50}Ti metal chip, while the ^{54}Cr [(99.8 ± 0.1)% enrichment] was obtained and used as a metal powder. The beams were delivered to the primary target chamber of the Momentum Achromat Recoil Spectrometer (MARS) [17] for the irradiation of ^{160}Gd (1.0 mg/cm^2 Gd_2O_3 on 2 μm Ti), ^{159}Tb (497 μg/cm^2 self-supporting), or ^{162}Dy (403 μg/cm^2 on 75 μg/cm^2 ^{nat}C) targets. The enriched (> 91%) ^{160}Gd target was prepared by molecular plating at Texas A&M University [18], the ^{159}Tb target was prepared by mechanical rolling and purchased from Microfoils Co., and the ^{162}Dy target was prepared by vacuum deposition. Two collimated ion-implanted Si detectors with an active area of 150 mm^2 were mounted horizontally at ±30^o to the beam axis and 241 mm away from the target position to monitor the luminosity (product of beam dose and target areal density) via elastic scattering. In addition, a Delrin cylinder with a center opening of 6.35 mm and a length of 21.6 mm was placed before each collimator to suppress transmission of scattering background particles. The absolute beam dose was calibrated with an electron-suppressed Faraday-cup placed directly downstream of the target. The energy of the primary beam was determined, with an estimated uncertainty of ≈1%, by passing it through a ^{nat}C foil (≈50 μg/cm^2) and measuring the magnetic rigidity of the beam ions in various charge states after MARS dipole D1. The ^{nat}C foil was mounted on the same ladder as the Faraday-cup and also used for charge equilibration of evaporation residues. A step-wise reduction of the primary beam energy was achieved using Al degraders with thicknesses in the range from 1.2 μm up to 8.54 μm. All energy loss calculations were done using LISE++ [19] according to the method of Ziegler *et al.* [20]. Fig. 1 shows a schematic of MARS and the principal experimental hardware.

The EvRs were separated from the primary beam and reaction byproducts using a two-stage selection criteria based on the particle's magnetic rigidity and velocity. MARS was tuned to transmit the most probable charge state of the residue as estimated according to Schiwietz and Grande [21] as implemented in LISE++. The transmission efficiency of MARS for heavy-ion recoils was experimentally characterized in [15] and later reevaluated in [2]. The EvRs were detected at the focal plane by an X1 design 16-strip position-sensitive silicon detector (PSSD) having an active area of 50 x 50 mm^2 purchased from Micron Semiconductor, Ltd. The energy and position calibration of the PSSD was performed with a four-peak α-source using ^{148}Gd, ^{239}Pu, ^{241}Am, and ^{244}Cm α-lines. A multi-slit Al mask, with slit width of 1 mm and interspacing of 8 mm, was used to calibrate the vertical position in each strip. The horizontal position resolution was defined by the 3 mm width of each strip. To correct for the contribution of the

daughter recoil energy to the α-decay energy of the EvR, an internal calibration using the products of the ^{50}Ti, ^{54}Cr+^{106}Pd (587 μg/cm^2 self-supporting) reactions was used.

Focal plane event discrimination, i.e., distinction between implantation and radioactive decay events in the PSSD, was accomplished by either pulsing the beam or, after a focal plane upgrade, by installing a large-area (44 cm^2) microchannel plate (MCP) detector upstream of the PSSD. The beam pulse duration was set to 50 ms for both the beam-on and beam-off periods. The pulsing was achieved by repeatedly de-phasing one of the K500 cyclotron dees by ≈10^o. The probability of observing EvR α-decays in the beam-off window apart from the background that accompanies the beam-on interval is ≈50%, as the product half-life typically exceeds the duration of the pulse period. In later experiments, the beam was *not* pulsed and the implanting ions were discriminated using the MCP signal. Coincident signals in the MCP and the PSSD indicated an implantation event, while radioactive decay events were seen only in the PSSD. The EvRs had to traverse the electrostatic grid of the MCP, which had an 85% transparency. The detection efficiency of the MCP was > 99%. The fractions of the EvR spatial distributions striking the PSSD detector were (100 ± 2)% and (85 ± 10)% in the horizontal and vertical directions, respectively, and the PSSD α-detection efficiency was (55 ± 3)%. The live-time of the acquisition system was typically > 99%, measured as a ratio of vetoed (when the system was busy processing data from a prior trigger event) and total scalar counts provided by a 1-MHz clock.

III. DATA ANALYSIS AND RESULTS

The EvRs of the present reactions were identified by their characteristic α-decay energies, which are known from literature [22] and are listed in Table I. In Fig. 2, individual α-spectra collected using MCP–PSSD event discrimination for the reactions ^{50}Ti+^{159}Tb and ^{50}Ti+^{162}Dy are shown. Some of the evaporation channel products overlap in decay energy, in which case their event count was combined and a sum cross section for the two channels is reported. An EvR-α_1-α_2 correlation search, where α_1 and α_2 are the α-events from the decay of parent and daughter nuclides, respectively, was performed to confirm the identity of the EvRs and to determine the corresponding number of decays of each product (when possible). Fig. 3 shows representative correlation search results for the 4*n* EvRs ^{205}Fr and ^{208}Ra (with possible contribution from the 5*n* EvR ^{207}Ra for the latter) from the ^{50}Ti+^{159}Tb and ^{50}Ti+^{162}Dy reactions, respectively. Correlated events had to occur in the same position, as defined by the horizontal (≈3 mm strip width) and vertical [15] position resolution of the PSSD. The search was constrained by a ±2 mm vertical position difference and by extending the time difference Δt_{max} to six half-lives between subsequent events, i.e., EvR-α_1 and α_1-α_2. For $\Delta t \geq 100$ s, randomly correlated events populate the spectra as seen in Figs. 3(a) and (b). The boxes in Figs. 3(c) and (d) are guides for the eyes and cover a position range of 2 mm, and an energy width of ± 60 keV around each α-decay

energy E_α. The identified number of EvR-α_1 correlations for ^{205}Fr of 47 (≈85 total after correcting for the PSSD α-detection efficiency) is consistent with 14 α_1-α_2 correlations since approximately half of the α-events escape the detector and the daughter nucleus ^{201}At has an α-decay branch of (71 ± 7)%. Likewise, the 17 identified EvR-α_1 correlations for ^{208}Ra are consistent with the subsequent 8 α_1-α_2 correlations, since the α-decay branch of its daughter nucleus ^{204}Rn is equal to (72.4 ± 0.9)%. By comparison, the number of events expected due to random correlations, i.e., between radioactive decays and implanted recoils that are unrelated, was calculated using the method in [23] to be < 0.8 for ^{205}Fr EvR-α_1 and < 0.2 for ^{208}Ra EvR-α_1 events. The number of calculated random correlations for the α_1-α_2 events are < 0.05 and < 0.01, compared to the 14 and 8 experimentally correlated events, respectively, as reported above. In these experiments, the average rate for α-like and EvR-like events was 0.04–0.07 min^{-1} and 5 min^{-1}, respectively. The measured lifetimes, τ_{meas}, for these 4*n* EvRs [shown in Figs. 3(a) and (b)] are 5.4 ± 0.8 s and 1.6 ± 0.2 s, in good agreement with the literature values of 5.7 ± 0.1 s and 1.9 ± 0.3 s for ^{205}Fr and ^{208}Ra, respectively [22]. This same correlation search analysis was used to confirm events from the remainder of the EvRs with short half-lives (≤ 30 s), for which the random correlation rates were comparably low.

The individual α-spectra collected at all incident projectile energies for the reaction ^{50}Ti+^{160}Gd are shown in Fig. 4. The EvRs produced in this reaction were too long-lived to perform a correlation search; when the half-life of the product is long, the probability of correlating unrelated events becomes considerable. To verify that the observed events are indeed due to radioactive decay and not fluctuation of background counts, a statistical test was performed. A per bin background count N_{bkgd} was determined by fitting the sum of the singles spectra shown in Fig. 4, assuming a flat background. Next, an expected number of background counts μ in an energy range defined by the PSSD resolution R_{PSSD} was calculated by taking the product of N_{bkgd} and the number of bins equivalent to the R_{PSSD}. Using Poisson statistics, the observed counts within R_{PSSD} were accepted with a ε = 95% confidence level as above background, if the number of counts was greater than the smallest integer *n* in the inequality

$$\sum_{j=0}^{n} \frac{\mu^j}{j!} e^{-\mu} \geq \varepsilon \,. \tag{1}$$

In summary, the observed peaks were considered above background only when their number of counts exceeded the 95% confidence limit of a cumulative Poisson distribution of background counts. After applying this confidence criterion to the ^{50}Ti+^{160}Gd data, only the 4,5*n* channel data passed this test and so only cross sections for these channels are reported. This same analysis was applied to the long-lived EvRs from charged-particle evaporation channels observed in the ^{50}Ti+^{159}Tb and ^{50}Ti+^{162}Dy reactions, which were also observed with low statistics. Subsequently, cross section data for the *p*2*n*+*p*3*n* and *p*4*n* channels from these systems were obtained.

The measured cross sections for the observed x*n* and *p*x*n* EvR channels in the ^{50}Ti+^{160}Gd, ^{159}Tb, ^{162}Dy and ^{54}Cr+^{162}Dy reactions are listed in Table II, with the errors representing statistical uncertainty. Due to the systematic uncertainty, the estimated absolute error of the measured cross sections is ±50%. The ^{54}Cr+^{162}Dy x*n* cross sections were below experimental sensitivity and the reported upper limits are calculated at a 84% confidence level [24]. The transition of products toward regions of greater neutron-deficit (lower proton binding energies) in reactions with heavier projectiles leads to greater contribution of the *p*x*n* channel to the total EvR cross section. For the ^{54}Cr+^{162}Dy reaction, the *p*2*n*+*p*3*n* cross sections exceed those for the 4*n*+5*n* channels, while their yield is more comparable in the ^{50}Ti+^{162}Dy reaction and is inverted for the ^{48}Ca+^{162}Dy reaction, where the x*n* channel dominates the EvR cross section (see Table II in the current work and Table II in [2]). Fig. 5 contrasts the x*n* excitation functions measured in the current work for the ^{50}Ti- and ^{54}Cr-induced reactions and those measured earlier for the ^{48}Ca-induced reactions with ^{159}Tb and ^{162}Dy. The maximum 4*n* (4*n*+5*n* in case of the latter) cross sections in the reactions ^{48}Ca+^{159}Tb and ^{48}Ca+^{162}Dy are 12.5 ± 2.0 mb and 12.7 ± 1.7 mb, respectively. With a shift to the heavier, higher-Z ^{50}Ti beam, the maximum 4*n* cross sections fall by factors of 26 and 74 to 481^{+173}_{-144} μb and 169^{+77}_{-60} μb for the reactions ^{50}Ti+^{159}Tb and ^{50}Ti+^{162}Dy, respectively. The largest 4*n* channel cross section for a ^{50}Ti reaction measured in the current work is 1060^{+380}_{-320} μb for the ^{50}Ti+^{160}Gd system, which is a factor of 12 below the 4*n* data for its ^{48}Ca+^{162}Dy cross-bombardment. The 4*n*+5*n* cross section in the ^{54}Cr+^{162}Dy reaction falls below 2–5 μb, a factor of more than 3×10^3 reduction relative to the maximum 4*n*+5*n* cross section measured for the ^{48}Ca+^{162}Dy reaction. The peak 4*n*+5*n* cross sections for the ^{54}Cr+^{162}Dy cross-bombardment reactions ^{40}Ar+^{176}Hf and ^{124}Sn+^{92}Zr are 174 ± 63 nb [9] and 53.4 ± 28.4 nb [25], respectively, and differ by only a factor of ≈3. The peak 4*n*+5*n* cross section for the more neutron-rich ^{54}Cr+^{164}Dy reaction is 3.50 ± 0.03 μb [26]. Combined, these data suggest that the peak 4*n* cross section for ^{54}Cr+^{162}Dy is likely below 1 μb.

IV. DISCUSSION

The fall of the macroscopic fission barriers [27] from approximately 9.3 MeV for $^{199\text{-}202}$Po isotopes in the ^{48}Ca reactions to approximately 4.7 MeV for $^{213\text{-}216}$Th isotopes in the ^{54}Cr reactions in part explains the steep decrease of the measured residue cross sections. It is necessary to quantify steps along the fusion-evaporation process, however, to gauge if this effect alone is sufficient to describe the data. To evaluate the cause for the substantial decrease of the x*n* production cross section in reactions with Z > 20 projectiles, the evaporation residue production cross section σ_{xn} can be estimated by modeling it as a product of three terms expressed formally as [28-31]:

$$\sigma_{xn} = \sigma_{cap}(E_{cm}, l) P_{CN}(E_{cm}, l) W_{xn}(E^*, l_{CN}), \quad (2)$$

where σ_{cap} is the capture cross section for production of a dinuclear projectile-target configuration in contact, the probability of compound nucleus formation P_{CN} quantifies the chance that the dinucleus will become an equilibrated mononucleus, and the survival probability W_{xn} leads to a ground-state residue following the evaporation of x neutrons in competition with fission. The dissimilar time scales of these processes permit this segmentation of the reaction into distinct stages and form the foundation of the compound nucleus model [32]. The details entering Eq. (2) were comprehensively presented in [2] and the same methodology is used here, so only a brief account of the model is given. The capture cross section is calculated using the "diffused barrier formula" derived by Świątecki *et al.* [33, 34], which uses a Gaussian distribution of barrier heights to describe the projectile-target interaction at sub-barrier energies. The energy-dependent estimates of P_{CN} are made using a semi-phenomenological expression reported in [35], which is a function of the Coulomb parameter $z = (Z_P Z_T) / (A_P^{1/3} + A_T^{1/3})$ with Z and A being the atomic and mass numbers, respectively, of either the projectile or target. This expression proved very satisfactory in modeling of the ^{48}Ca-induced reactions after scaling, which was guided by literature data, of the predicted P_{CN} (see discussion in [2] for details) and is extended to the calculations performed here to be consistent with this previous work. P_{CN} is the least well-understood component of Eq. (2) and estimates of its uncertainty can reach up to one order of magnitude [35-37]. In contrast, the cross section data described here span several orders of magnitude, even though the variation in z among the present reactions is relatively small and estimates of P_{CN} for the investigated systems are all within a factor of 3 at E^*_{CN} = 50 MeV. The decrease in cross section is best accounted for by considering the influence of the survival probability, the calculation of which is discussed next.

The calculation of the survival probability is performed using the closed-form expression derived from transition-state theory by Vandenbosch and Huizenga [38], with the Fermi-gas approximation for the level density, and by adapting methods described by Siwek-Wilczyńska *et al.* [29]. Furthermore, the recommendations of Swiek-Wilczyńska and Wilczyński [39], and Świątecki *et al.* [40], with respect to the calculation of fission barrier height and the shell correction in the neutron emission rate, are followed. The Vandenbosch and Huizenga expression gives the ratio of the decay widths Γ_n and Γ_f for the neutron emission and fission channels, respectively. The magnitude of each decay width is proportional to the nuclear level density integrated from the transition state, i.e., the daughter nucleus in neutron emission at energy S_n and saddle-point in fission at energy B_f, up to the excitation energy of the CN. The S_n and B_f denote the neutron separation energy and fission barrier, respectively. Due to the induced spin of the CN and the restriction imposed by the yrast line on the minimum accessible excitation energy at a give spin, the thermal energy $U = E^*_{CN} - E_{rot}$ is used in the calculations [29]. The moderate to high fissility of nuclides near and above the N = 126 shell reduces the contribution of higher spin

states to the EvR cross section. This defines an upper limit for the maximum sustainable angular momentum l_{cr}, which is below the maximum l attainable in the entrance channel [41, 42]. The moment of inertia is estimated as suggested in [8], using the rigid-body expression $J = \frac{2}{5} m_o A R^2 (1 + \beta_2 / 3)$, where m_o = 931.494 MeV/c^2, $R = 1.2A^{1/3}$ fm, and β_2 is the quadrupole deformation parameter. The level density parameters a_n and a_f are calculated using the parameterization of Reisdorf [43], with the influence of shell effects on the level density included using the formalism of Ignatyuk *et al*. [44]. The neutron separation energies were taken from [22], while the fission barrier was calculated as a macroscopic-microscopic sum of the finite-range rotating-liquid-drop (FRLD) model $B_{f,LD}(l)$ [27, 45] and the shell correction energy, δS, was taken from M□ller *et al.* [46]. Furthermore, an option to include the influence of collective excitations on the level density is incorporated into the model, with the formalism of Zagrebaev *et al.* [31, 47] used to describe the collective enhancements of level density and with its fade-out regulated by the parameters determined in [8]. The overall collective enhancement is taken as a sum of rotational and vibrational terms, and multiplies the single-particle level density described by the Fermi-gas approximation. The resulting model composed of these united components was evaluated in [2] with a satisfactory outcome and is based on earlier works where a similar model approach was successfully applied to describe heavy-ion fusion reaction data [28, 29]. Fission delay due to dynamical dissipation effects [48, 49] is neglected in the calculations, as this phenomenon is generally shown [50, 51] to be most significant at excitation energies above the maxima of the 3*n* and 4*n* excitation functions (≳50 MeV). Investigations are ongoing to improve our understanding of these dynamical effects and on their role in heavy-ion fusion [30, 52, 53].

Fig. 6 shows the measured 4*n* excitation functions in the ^{50}Ti+^{160}Gd, ^{159}Tb, and ^{162}Dy reactions. The measured 4*n* excitation functions in the ^{48}Ca+^{159}Tb, ^{162}Dy reactions are also plotted for comparison, where the ^{48}Ca+^{162}Dy system is a cross-bombardment for the ^{50}Ti+^{160}Gd reaction. The predictions for these excitation functions using the model discussed above are represented by the curves, which underestimate the ^{50}Ti+^{159}Tb,^{162}Dy reaction data. A major uncertainty in the calculations of survival probability comes from lack of experimental data on fission barrier heights, B_f, relevant to the present reactions. On the other hand, predictions for the ^{50}Ti+^{160}Gd reaction overestimate the data by approximately a factor of 5. Since this latter system leads to the same CN as the ^{48}Ca+^{162}Dy reaction, this discrepancy could be due to an error in the entrance channel of the model calculations, e.g., overestimated P_{CN}, or another effect. It should be noted that during the relevant experiment, the electrical current in the beamline magnets upstream of MARS intermittently drifted, which could have affected the focus of the ^{50}Ti beam and the angular distribution of recoils in the relevant runs. Although the change in current was slight, it may be instructive to confirm the measured cross sections for the ^{160}Gd(^{50}Ti,x*n*) reactions in the future.

All of the model predictions in Fig. 6 include the CELD effect. The significance of this effect for the present systems is illustrated in Fig. 7, where the maximum measured 4*n* or 4*n*+5*n* cross section data from the ^{48}Ca, ^{50}Ti, and ^{54}Cr reactions are plotted along with model predictions excluding (solid line) and including (dashed line) CELD. The abscissa is the mean difference $\overline{B_f - S_n}$ for products along the CN deexcitation cascade up to the 4*n* EvR, where S_n is the neutron separation energy. The data points below the ^{54}Cr+^{162}Dy upper limit serve as reasonable range markers of its expected 4*n*+5*n* cross section and correspond to the maximum 4*n*+5*n* cross sections of the cross-bombardment reactions ^{40}Ar+^{176}Hf and ^{124}Sn+^{92}Zr as discussed at the end of Sec. III. The scarce availability of experimental fission barriers, especially for neutron-deficient nuclides, make it a considerable source of uncertainty entering the calculations. This problem is amplified in hot fusion by the occurrence of multi-chance fission as the CN de-excites. The gray boundaries represent the uncertainty in the prediction of the cross sections due to a ±0.5 MeV uncertainty of the estimated FRLD $B_{f,LD}$ [45]. The data in Fig. 7 are reproduced satisfactorily, across nearly five orders of magnitude, by the inclusion of the enhancement of nuclear level density by collective excitations and the consideration of the uncertainty of $B_{f,LD}$. Otherwise, the model overestimates the data by 0.5–2 orders of magnitude. When changing the projectile from ^{48}Ca to ^{50}Ti to ^{54}Cr, the resulting decrease in $\overline{B_f - S_n}$ is roughly synonymous with an increase in the fissility of the products. The effect on the resulting EvR cross sections is especially pronounced when $\overline{B_f - S_n}$ is small, since $\Gamma_n << \Gamma_f$ and any increase in Γ_f will substantially reduce W_{xn}. Although charged-particle evaporation was neglected in the model calculations, more comprehensive theoretical calculations [47] inclusive of all major evaporation channels similarly overestimate the measured excitation functions and likewise point to the significance of the CELD effect. This was demonstrated in the analysis of the ^{48}Ca data in [2] and is discussed in the context of the present ^{50}Ti data in [54]. In summary, competition from proton and alpha evaporation is not sufficient to explain the unexpectedly low production cross sections measured here without considering other factors such as CELD.

The present work concerns reaction phenomena that arise in the deexcitation of a hot CN as a result of the nuclear properties exhibited by spherical, shell-stabilized nuclides. Despite the proximity of the EvRs to the N = 126 shell, an unexpectedly low stabilizing influence on the survival probability is deduced from the measured x*n* production cross sections in the current work. The cause of this is attributed to the role of CELD in the deexcitation of the CN. This observation supports the findings of an earlier report [8], where the anticipated susceptibility of nuclei near the predicted N =184 shell closure to CELD was also discussed. Attempts to synthesize spherical SHEs in that region have not yet shown indications for enhanced stability against fission [5, 7], even though there is evidence that the procession toward N = 184 is accompanied by an increase in nuclide stability in the ground state [3]. This information is

consistent with the present results for N = 126, and leads to the conclusion that collective phenomena, *along* with low fusion probabilities of relevant projectile and target combinations [55], may complicate the search for elements with $Z \geq 118$ near $N = 184$. For now, continued experimental efforts are essential to evaluate and characterize mechanistic phenomena in fusion-evaporation, with additional data needed to reduce uncertainties in the description of low-energy heavy-ion fusion reactions [36].

V. CONCLUSION

Production cross sections of shell-stabilized nuclides with Z = 86–90 and in the vicinity of the N = 126 shell were measured in ^{50}Ti- and ^{54}Cr-induced reactions with lanthanide ^{160}Gd, ^{159}Tb, and ^{162}Dy targets. The x*n* cross sections provide information on the competition between neutron emission and fission in the deexcitation of the compound nucleus, thus on the transition state level density of each channel. Despite significant ground-state shell correction energies of the EvRs, a model-dependent analysis of the measured x*n* data suggests a rather weak influence of pronounced microscopic shell structure on stabilizing the products against fission. Instead, the measured data is best modeled by enhancing the fission probability. The inclusion of CELD in the calculations permits a satisfactory modeling of the measured data across nearly five orders of magnitude. The coupling of rotational excitations to single-particle states as the excited nucleus approaches the fission saddle-point configuration enhances the fission level density, while much smaller vibrational enhancement affects the neutron emission rate for spherical nuclei. The current results support some previous findings and warrant additional experimental work on the nature and implication of the CELD effect.

VI. ACKNOWLEDGEMENTS

The authors would like to thank the Cyclotron Institute accelerator group (D. P. May, G. J. Kim, and B. T. Roeder) for developing and delivering stable beams of ^{50}Ti and ^{54}Cr. We thank J. P. Greene for the $^{50}TiO_2$ reduction, and the Heavy Elements Group at Lawrence Berkeley National Laboratory for providing the ^{162}Dy target and the designs for the molecular plating cell used to fabricate the ^{160}Gd target. We further express sincere gratitude to K. Siwek-Wilczyńska and to the NRV group at the Flerov Laboratory of Nuclear Reactions at the Joint Institute for Nuclear Research in Dubna, Russia for valuable private communications regarding their respective theoretical models. This material is based upon work supported by the U.S. Department of Energy, Office of Science, Office of Nuclear Physics under Award Numbers DE-FG02-93ER40773, DE-FG02-12ER41869/DE-SC0008126, and DE-FG07-05ID14692/MUSC09-100. Additionally, this work was supported by the Robert A. Welch Foundation under award number A-1710, and the Texas A&M University College of Science.

REFERENCES

[1] N. Bohr and J. A. Wheeler, Phys. Rev., **56**, 426 (1939).
[2] D. A. Mayorov *et al.*, Phys. Rev. C, **90**, 024602 (2014).
[3] J. H. Hamilton, S. Hofmann, and Y. T. Oganessian, Annu. Rev. Nucl. Part. Sci., **63**, 383 (2013).
[4] Y. T. Oganessian and V. K. Utyonkov, Rep. Prog. Phys., **78**, 036301 (2015).
[5] S. Hofmann *et al.*, GSI Scientific Report No. NUSTAR-SHE-01, edited by K. Große, 2009, p. 131.
[6] J. Khuyagbaatar *et al.*, GSI Scientific Report No. PHN-ENNA-EXP-01, edited by K. Große, 2013, p. 131.
[7] Y. T. Oganessian *et al.*, Phys. Rev. C, **79**, 024603 (2009).
[8] A. R. Junghans *et al.*, Nucl. Phys. A, **629**, 635 (1998).
[9] D. Vermeulen *et al.*, Z. Phys. A, **318**, 157 (1984).
[10] A. Heinz *et al.*, Nucl. Phys. A, **713**, 3 (2003).
[11] P. Roy *et al.*, Phys. Rev. C, **88**, 031601 (2013).
[12] V. Singh *et al.*, Phys. Rev. C, **89**, 024609 (2014).
[13] S. Komarov *et al.*, Phys. Rev. C, **75**, 064611 (2007).
[14] R. N. Sagaidak and A. N. Andreyev, Phys. Rev. C, **79**, 054613 (2009).
[15] C. M. Folden III *et al.*, Nucl. Instrum. Methods A, **678**, 1 (2012).
[16] B. Lommel *et al.*, J. Radioanal. Nucl. Chem., **299**, 977 (2014).
[17] R. E. Tribble, R. H. Burch, and C. A. Gagliardi, Nucl. Instrum. Methods A, **285**, 441 (1989).
[18] T. A. Werke *et al.*, Cyclotron Institute Progress in Research Report 2014: Superconducting Cyclotron, Instrumentation and RIB Upgrade, edited by Y.-W. Lui, 2014, p. IV48.
[19] O. B. Tarasov and D. Bazin, Nucl. Instrum. Methods B, **266**, 4657 (2008).
[20] J. F. Ziegler, J. P. Biersack, and U. Littmark, *The Stopping and Range of Ions in Solids* (Pergamon Press, New York, 1984).
[21] G. Schiwietz and P. L. Grande, Nucl. Instrum. Methods B, **175**, 125 (2001).
[22] NNDC, Chart of the Nuclides: Basic Properties of Atomic Nuclei, available at http://www.nndc.bnl.gov.
[23] C. M. Folden III *et al.*, Phys. Rev. C, **73**, 014611 (2006).
[24] K.-H. Schmidt *et al.*, Z. Phys. A, **316**, 19 (1984).
[25] C. C. Sahm *et al.*, Nucl. Phys. A, **441**, 316 (1985).
[26] J. Khuyagbaatar *et al.*, Eur. Phys. J. A, **34**, 355 (2007).
[27] A. J. Sierk, Phys. Rev. C, **33**, 2039 (1986).
[28] W. Loveland, Phys. Rev. C, **76**, 014612 (2007).
[29] K. Siwek-Wilczyńska, I. Skwira, and J. Wilczyński, Phys. Rev. C, **72**, 034605 (2005).
[30] R. Yanez *et al.*, Phys. Rev. Lett., **112**, 152702 (2014).
[31] V. I. Zagrebaev *et al.*, Phys. Rev. C, **65**, 014607 (2001).
[32] N. Bohr, Nature, **138**, 344 (1936).

[33] W. J. Świa□tecki, K. Siwek-Wilczyńska, and J. Wilczyński, Acta Phys. Pol. B, **34**, 2049 (2003).
[34] W. J. Świątecki, K. Siwek-Wilczyńska, and J. Wilczyński, Phys. Rev. C, **71**, 014602 (2005).
[35] K. Siwek-Wilczyńska *et al.*, Int. J. Mod. Phys. E, **17**, 12 (2008).
[36] W. Loveland, Eur. Phys. J. A, **51**, 1 (2015).
[37] R. Yanez *et al.*, Phys. Rev. C, **88**, 014606 (2013).
[38] R. Vandenbosch and J. Huizenga, *Nuclear Fission* (Academic, New York, 1973).
[39] K. Siwek-Wilczyńska and J. Wilczyński, Intl. J. Mod. Phys. E, **18**, 823 (2009).
[40] W. J. Świa□tecki, K. Siwek-Wilczyńska, and J. Wilczyński, Phys. Rev. C, **78**, 054604 (2008).
[41] A. N. Andreyev *et al.*, Phys. Rev. C, **72**, 014612 (2005).
[42] G. Henning *et al.*, Phys. Rev. Lett., **113**, 262505 (2014).
[43] W. Reisdorf, Z. Phys. A, **300**, 227 (1981).
[44] A. V. Ignatyuk *et al.*, Sov. J. Nucl. Phys., **21**, 612 (1975).
[45] A. J. Sierk, Fisrot: Code for Liquid Drop Fission Barriers, available at https://www-nds.iaea.org/RIPL-3/.
[46] P. Möller *et al.*, Atom. Data Nucl. Data Tables, **59**, 185 (1995).
[47] V. I. Zagrebaev *et al.*, Fusion-Evaporation Codes of NRV, available at http://nrv.jinr.ru/nrv/.
[48] D. Jacquet and M. Morjean, Prog. Part. Nucl. Phys., **63**, 155 (2009).
[49] H. A. Kramers, Physica, **7**, 284 (1940).
[50] B. B. Back *et al.*, Phys. Rev. C, **60**, 044602 (1999).
[51] M. Thoennessen and G. F. Bertsch, Phys. Rev. Lett., **71**, 4303 (1993).
[52] K. Mahata, S. Kailas, and S. S. Kapoor, arXiv:1504.02599 [nucl-ex] (2015).
[53] E. Prasad *et al.*, Phys. Rev. C, **84**, 064606 (2011).
[54] D. A. Mayorov, Ph.D. Thesis, Texas A&M University, 2015.
[55] A. K. Nasirov *et al.*, Phys. Rev. C, **84**, 044612 (2011).
[56] K.-H. Schmidt, Eur. Phys. J. A, **8**, 141 (2000).

TABLE I. Nuclear decay properties of observed EvRs from evaporation channels populated in ^{50}Ti and ^{54}Cr reactions in this work. The literature values are taken from [22] and references therein.

Target	EvR (Chan.)	$E_{\alpha,\,obs}$ (keV)	$E_{\alpha,\,lit}$ (keV)	$I_{\alpha,\,lit}$ (%)	$t_{1/2,lit}$
^{50}Ti-Induced Reactions					
^{160}Gd	^{207}Rn (3*n*)	Not Observed	6131 ± 4	20.8 ± 3.0	9.25 ± 0.17 min
	^{206}Rn (4*n*)	6263 ± 5[a]	6259.7 ± 1.6	63 ± 6	5.67 ± 0.17 min
	^{205}Rn (5*n*)		6261.4 ± 1.8	24.2 ± 0.9	2.83 ± 0.07 min
^{159}Tb	^{206}Fr (3*n*)	6802 ± 7	6792 ± 5	84 ± 2	15.9 ± 0.3 s
	^{205}Fr (4*n*)	6934 ± 3	6915 ± 1	100 ± 2	3.92 ± 0.04 s
	^{204}Fr (5*n*)	7053 ± 13	7031 ± 5	69.6 ± 15.0	1.9 ± 0.5 s
	^{206}Rn (*p*2*n*)	6250 ± 15[a]	6259.7 ± 1.6	63 ± 6	5.67 ± 0.17 min
	^{205}Rn (*p*3*n*)		6261.4 ± 1.8	24.2 ± 0.9	2.83 ± 0.07 min
	^{204}Rn (*p*4*n*)	6408 ± 8	6418.9 ± 1.4	72.4 ± 0.9	1.23 ± 0.02 min
^{162}Dy	^{209}Ra (3*n*)	7004 ± 8	7003 ± 10	99.3[b]	4.7 ± 0.2 s
	^{208}Ra (4*n*)	7144 ± 9[a]	7133 ± 5	95 ± 5	1.3 ± 0.2 s
	^{207}Ra (5*n*)		7131 ± 4	100[b]	1.2 ± 0.1 s
	^{209}Fr (*p*2*n*)	6650 ± 18[a]	6646 ± 5	89 ± 3	50.5 ± 0.7 s
	^{208}Fr (*p*3*n*)		6641 ± 3	89 ± 3	59.1 ± 0.3 s
^{54}Cr-Induced Reactions					
^{162}Dy	^{212}Th (4*n*)	Not Observed	7802 ± 10	99.7 ± 0.3	30^{+20}_{-10} ms
	^{211}Th (5*n*)		7792 ± 14	100[b]	37^{+28}_{-11} ms
	^{213}Ac (*p*2*n*)	7347 ± 27[c]	7364 ± 8	100[b]	0.80 ± 0.05 s
	^{212}Ac (*p*3*n*)		7379 ± 8	97[b]	0.93 ± 0.05 s

[a]Measured centroid for two neighboring, indistinguishable evaporation channels.

[b]Uncertainty not reported.

[c]Uncertainty corresponds to the sample standard deviation.

TABLE II. Measured EvR production cross sections in the lanthanide target-based ^{50}Ti- and ^{54}Cr-induced reactions. The upper limits are calculated at an 84% confidence level [24].

Evaporation Channel	$E_{lab,cot}$ (MeV)	σ_{EvR} (μb)	Evaporation Channel	$E_{lab,cot}$ (MeV)	σ_{EvR} (μb)
^{50}Ti + ^{159}Tb			^{50}Ti + ^{162}Dy	Continued	
3*n*	207	334^{+168}_{-125}	4*n*+5*n*	209	51^{+119}_{-45}
	210	213^{+165}_{-114}		213	159^{+87}_{-66}
	214	76^{+102}_{-52}		219	169^{+77}_{-60}
	221	41^{+47}_{-24}		222	53^{+38}_{-32}
	223	51^{+61}_{-31}			
	228	22^{+43}_{-16}	*p*2*n*+*p*3*n*	209	160^{+150}_{-98}
				213	49^{+57}_{-23}
4*n*	207	120^{+111}_{-60}		219	88^{+80}_{-42}
	210	403^{+191}_{-149}			
	214	481^{+173}_{-144}	^{50}Ti + ^{160}Gd		
	221	384^{+125}_{-116}	4*n*+5*n*	202	325^{+199}_{-147}
	224	119^{+60}_{-45}		207	590^{+253}_{-203}
	228	34^{+27}_{-18}		211	1060^{+380}_{-320}
				214	611^{+264}_{-212}
5*n*	220	131^{+85}_{-61}		217	590^{+284}_{-222}
	223	66^{+74}_{-39}		224	185^{+128}_{-91}
	228	30^{+59}_{-23}			
			^{54}Cr + ^{162}Dy		
*p*2*n*+*p*3*n*	214	150^{+140}_{-90}	4*n*+5*n*	243	< 5
				248	< 3
*p*4*n*	220	90^{+110}_{-70}		253	< 2
	224	190^{+150}_{-100}			
			*p*2*n*+*p*3*n*	243	5^{+7}_{-3}
^{50}Ti + ^{162}Dy				248	< 2
3*n*	209	110^{+150}_{-67}		253	2^{+3}_{-2}
	213	270^{+110}_{-90}			
	219	156^{+85}_{-66}			
	222	41^{+54}_{-28}			

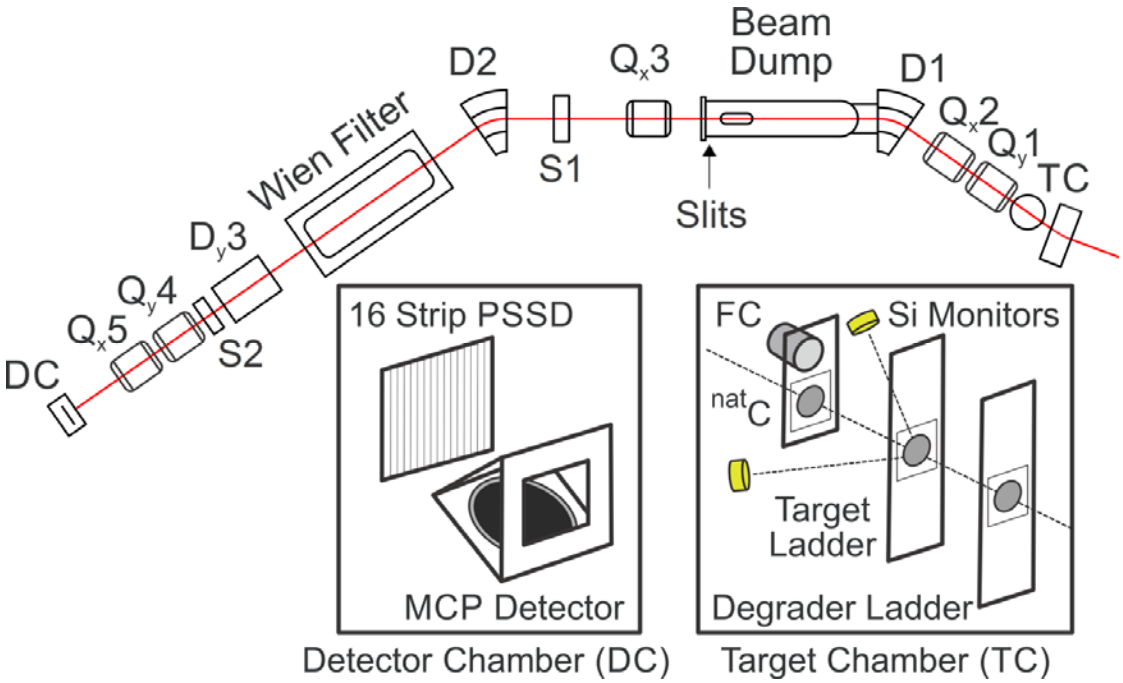

FIG. 1. (color online) Schematic layout of MARS, with the target and detector orientations in the target chamber and detector chamber, respectively, shown in the outlined panels. The dipole and quadrupole magnets are labeled by D and Q, respectively, by a subscript and/or number denoting the focusing plane and downstream position. Sextupole magnets are labeled by S1 and S2. The "Slits" define the momentum acceptance of the spectrometer.

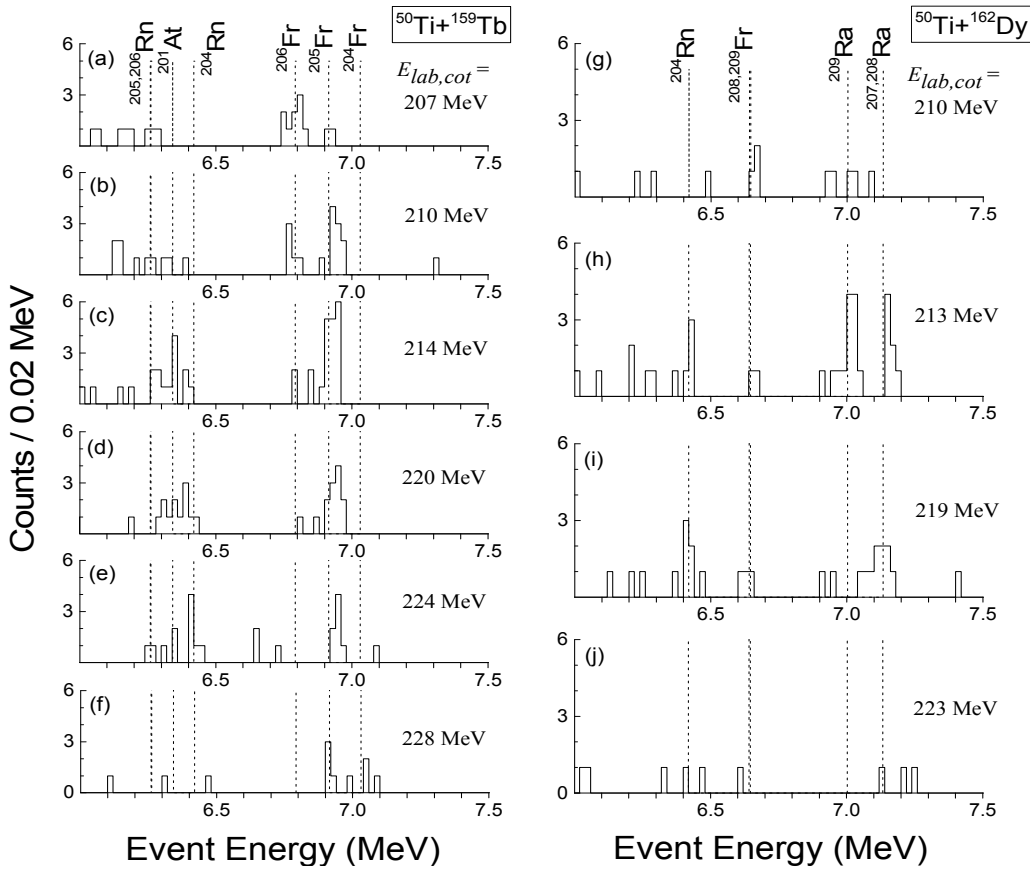

FIG. 2. Spectra of radioactive decay events for the reactions ^{50}Ti+^{159}Tb, panels (a)–(f), and ^{50}Ti+^{162}Dy, panels (g)–(j), observed in the PSSD. The data are from an experiment where an MCP detector was used for focal plane event discrimination. The vertical lines indicate known alpha decay energies for EvRs anticipated from the x*n* and *p*x*n* evaporation channels, and their α-decay daughter nuclides. $E_{lab,cot}$ represents the laboratory-frame center-of-target projectile energy.

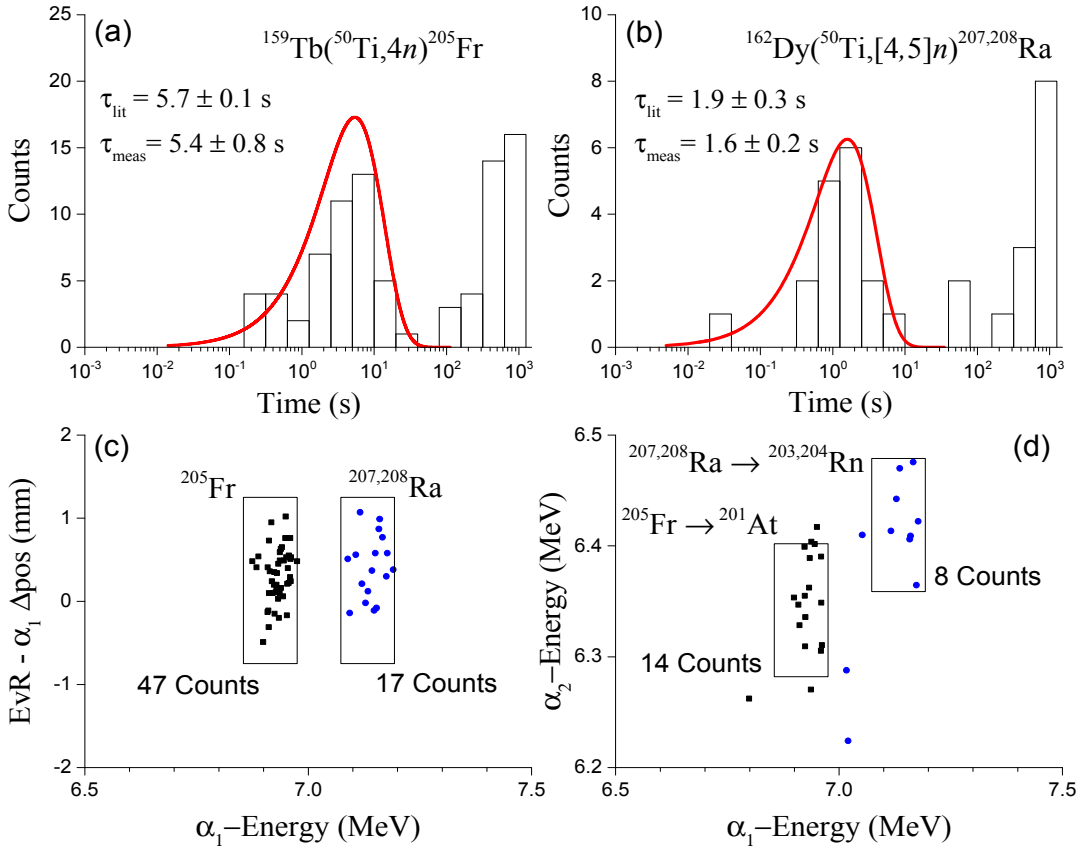

FIG. 3. (color online) EvR-α_1-α_2 correlation search result for the short-lived 4n EvRs ^{205}Fr and ^{208}Ra produced in the reactions ^{50}Ti + ^{159}Tb and ^{50}Ti + ^{162}Dy, respectively. Panels (a) and (b) show the measured logarithmic lifetime distributions for ^{205}Fr and ^{208}Ra, respectively. The values of τ_{meas} are obtained from the fit to the data shown by the curves using Eq. (8) from [56], while τ_{lit} is the literature lifetime from [22]. The maximum time between events in the top panels was set to 10^3 s, with the counts above approximately 10^2 s corresponding to randomly correlated events. The correlated EvR-α_1 and α_1-α_2 events within a time window corresponding to $6t_{1/2}$ of the decaying nuclide and within a position difference $\Delta pos = \pm 2$ mm are shown in panels (c) and (d). Only the correlations with $\Delta t < 30$ s (real correlations) from panels (a) and (b) are shown in panel (c). The boxes are included to guide the eye and cover a position range of 2 mm [panel (c)], and an energy width of ±60 keV about each α-decay energy E_α [panels (c) and (d)]. The α_1-α_2 correlation search was conducted over the decay energy ranges shown by the axes.

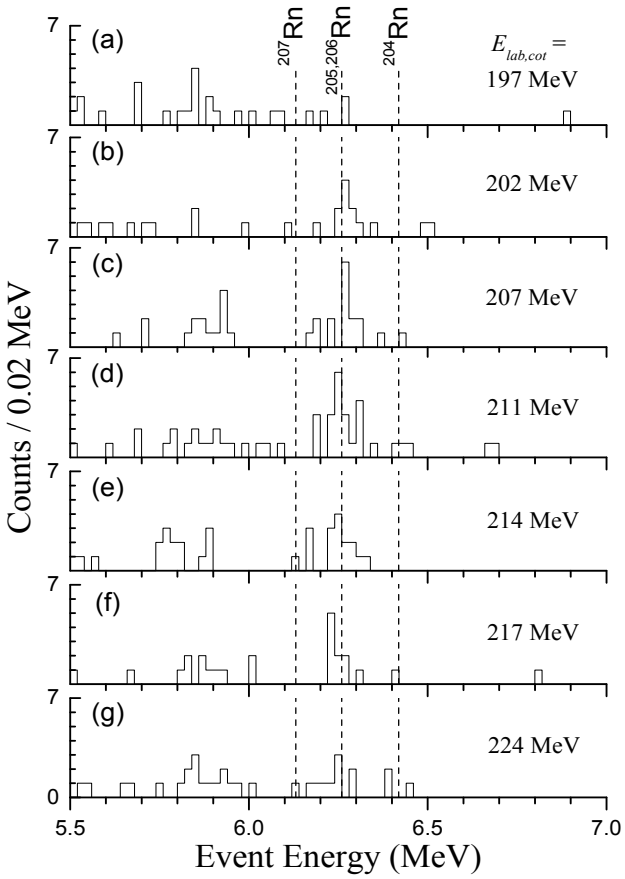

FIG. 4. Spectra of radioactive decay events for the reaction ^{50}Ti + ^{160}Gd observed in the PSSD. The vertical lines intersect known alpha decay energies for Rn isotopes. $E_{lab,cot}$ represents the laboratory-frame center-of-target projectile energy. The events populating the region from 5.5–6.0 MeV is predominantly due to beam-induced and chamber contamination background [2].

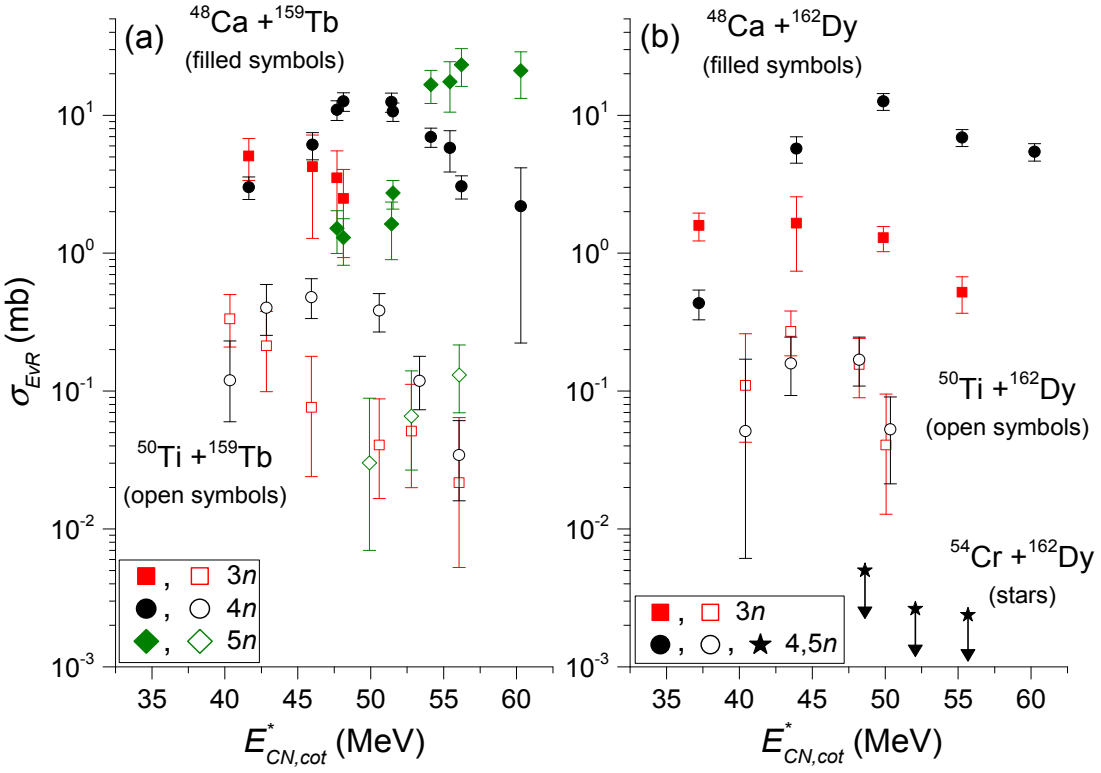

FIG. 5. (color online) Measured x*n* residue excitation functions for reactions induced by ^{48}Ca [2], ^{50}Ti, or ^{54}Cr on either the ^{159}Tb or ^{162}Dy target. Upper limits for ^{54}Cr + ^{162}Dy were calculated at an 84% confidence level. The abscissa is presented in terms of the CN excitation energy at the center-of-target.

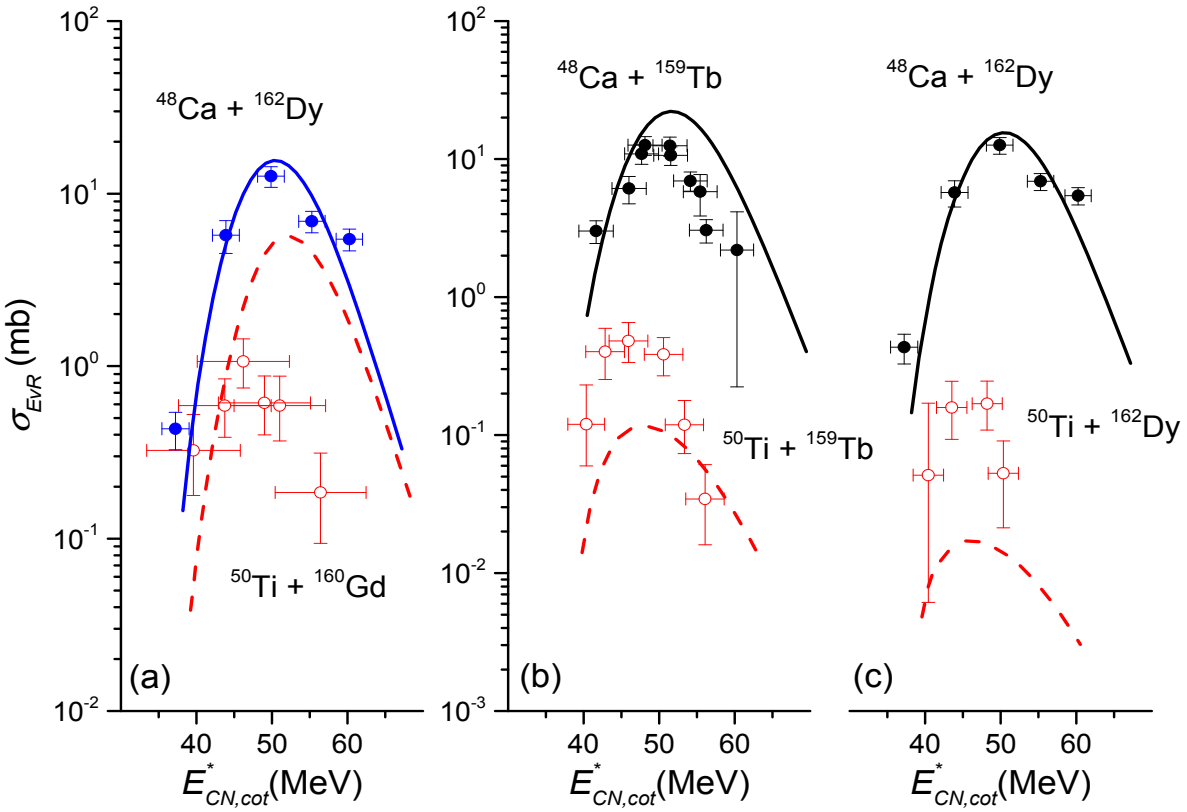

FIG. 6. (color online) Experimental data and theoretical predictions for the 4*n* excitation functions in the ^{48}Ca+^{159}Tb,^{162}Dy and ^{50}Ti+^{160}Gd, ^{159}Tb, ^{162}Dy reactions. Symbols indicate experimental results, meanwhile the solid and dashed curves show model calculations including CELD. The ^{48}Ca+^{162}Dy and ^{50}Ti+^{160}Gd reactions in panel (a) are a cross-bombardment leading to the same CN ^{210}Rn and 4n EvR. Panels (b) and (c) show ^{48}Ca- and ^{50}Ti-induced reactions with the same targets. Horizontal error bars represent the energy uncertainty due to target thickness. The ^{50}Ti+^{160}Gd data may have been affected by experimental difficulties (see main text), which is a possible source of discrepancy between the model and measurement.

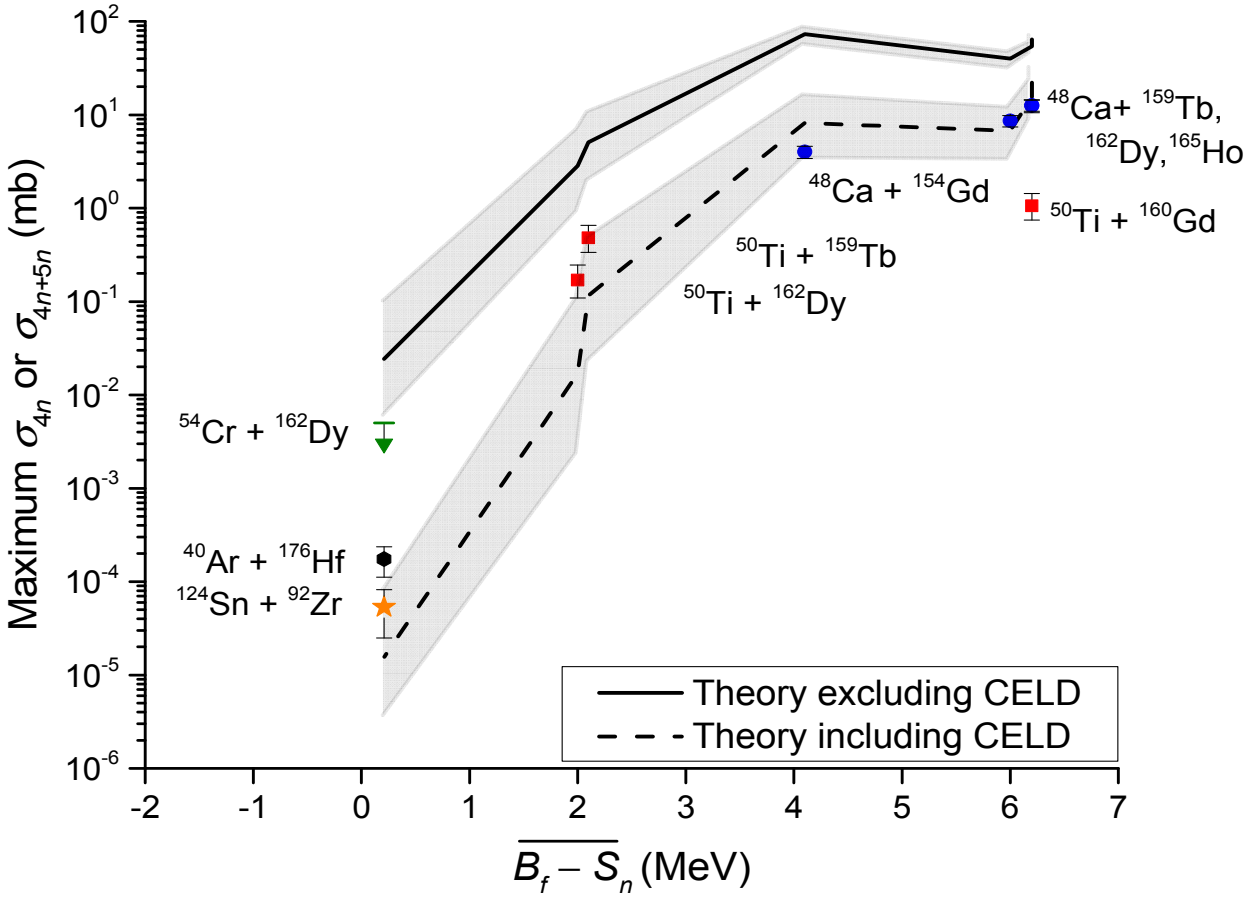

FIG. 7. (color online) Maximum 4*n* or 4*n*+5*n* cross section, or upper limit, measured in the lanthanide-based reactions with ^{48}Ca, ^{50}Ti, and ^{54}Cr projectiles. The data is plotted as a function of the mean value $\overline{B_f - S_n}$, which includes the deexcitation steps from the CN to the 4*n* EvR. The vertical gray bands show the uncertainty of the calculated cross sections due to a ±0.5 MeV uncertainty of $B_{f,LD}$. The data points below the upper limit are maximum 4*n*+5*n* cross sections measured in the ^{54}Cr+^{162}Dy cross-bombardment reactions ^{40}Ar+^{176}Hf [9] and ^{124}Sn+^{92}Zr [25], and serve as estimates for the expected magnitude of $\sigma_{4n,max}$ for the ^{54}Cr system (see the main text for details). The deviation of the ^{50}Ti+^{160}Gd data is addressed in the main text.